Vol.2010-CVIM-172 No.37
2010/5/28

Reflectance Analysis of Layered Surfaces Using Spectral Information

Tetsuro Morimoto,[†1] Rei Kawakami[†1]
and Katsushi Ikeuchi[†1]

It is important to understand how to use digital data to preserve the meaningful information about cultural heritages, including their shape and surface color. This paper introduces the development of novel multispectral imaging systems for modeling the color information for cultural heritages, proposing reflectance analysis methods using a multispectral image, and applying them in practice.

1. Introduction

Despite great public interest in cultural heritages, knowledge of these heritages is often restricted because of the possibility of deterioration and collapse. Consequently, it has become an important goal in the computer science community to model and record these restricted heritages and then use the digital data associated with such heritages in a variety of ways. For example, digital data is used to create digital media such as computer graphics CG)[7] and virtual reality (VR) content[11]. It is also used for analysis that can aid in the restoration and preservation of cultural heritages.

Therefore, it is important to understand how to use this digital data to preserve the important information about cultural heritages, including their shape and surface color. Usually, shape information can be obtained by a laser range sensor, and this information has become more accessible with improved data processing algorithms[7]. However, current color imaging systems like digital still camera (DSC) are usually represented with the traditional red, green, blue (RGB) color model. RGB cannot always provide accurate color information. The color of images captured with DSC is dependent on both the characteristics of the device and the condition of the illumination environment, making it difficult to accurately represent color appearance in the real world. Consequently, we need to capture surface spectral reflectance as ultimate color information in order to preserve the accurate color of cultural heritages.

Spectral reflectance is inherent in the nature of objects. Object analysis using the fact that different materials have different spectral reflectance is performed in many fields, such as medical imaging, agriculture, archaeology, and art. However, in the real world, it is difficult to obtain and handle a multispectral image effectively. Many objects are often found in an outdoor environment or in a dark environment, and these can pose problems. In an outdoor environment, for instance, the illumination environment changes greatly from one time to another. This causes saturation and underexposure when measuring the spectra. Moreover, many objects have at their surface complex reflection, absorption, and scattering, with a color mixture between the top and bottom layers, making material segmentation impossible. This paper targets analysis of cultural heritages having such multilayered characteristics.

Our goal is development of novel multispectral imaging systems for the color of modeling cultural heritages, proposing reflectance analysis methods using a multispectral image, and applying them in practice. The paper proposes the following three tasks related to preservation, release, and analysis.

The structure of this paper is as follows. In section2, we propose a practical color restoration method based on spectral information. In order to make VR contents by using 3D data, texture images by DSC are generally used as color information. However, the color of images captured with DSC is dependent on both the characteristics of the device and the condition of the illumination environment, and often the color information is not accurate. In a narrow environment, such as a tumulus, compact mobility is necessary to measure spectra. For these circumstances, we propose a color restoration method that uses both high resolution images captured by DSC and spectral information captured by a conventional spectrometer. This is a practical method from the viewpoint of automation and computational cost. In section3, we propose an efficient method for acquiring and segmenting multispectral images captured in outdoor environments. A conventional multispectral imaging system may have two kinds of

†1 The University of Tokyo

cameras. The first is a multiband camera[18], which is mainly used in the color reproduction field and does not have high spectral resolution, but has high image quality. The second is a hyperspectral sensor[4], which is mainly used in the aerial remote sensing field and does not have high image quality, but has high spectral resolution. Compared to these systems our solution has not only high image quality and sufficient spectral resolution for object analysis but also a wide capture angle. The multispectral image segmentation method can handle object surfaces having complex reflection based on a statistical procedure. In section 4, a novel physical model, the so-called "Spider" model, which can be used to estimate the optical properties of layered surfaces, is proposed. Many object surfaces such as wall paintings are composed of layers of different physical substances, and are called "layered surfaces." Such surfaces have more complex optical properties than a diffuse surface and are generally unable to be segmented. For this reason, we propose the Spider model to analyze the complex optical properties of layered surfaces. We also develop a novel method that can not only segment the surfaces but also decompose the optical properties of layered surfaces.

2. Color Restoration Method Based on Spectral Information

In this section, we introduce a novel method for color restoration that can effectively and simplily apply accurate color based on spectral information to a segmented image using the Normalized Cuts technique[16]. Using the proposed method, we can obtain a digital still camera image and spectral information in different environments. Also, it is not necessary to estimate reflectance spectra using a spectral database such as those that are used in other methods[18]. The synthesized images have accurate color and high resolution. The proposed method works effectively when applied to digital archive contents.

2.1 DSC Image Segmentation using Normalized Cuts Method

We employ image segmentation using the NCuts method to apply spectral information into the DSC image effectively, since NCuts can handle the mixture of pigment and rock. Furthermore, we use a slight improvement to divide the imaged DSC into multiple groups[2]. First of all, we create the feature vector as follows: $F(i) = [a_i^*, b_i^*, x_i, y_i], \quad i = 1, 2, 3, \cdots, N$, where x and y are the horizontal and vertical positions of image pixels, N is the number of samples, and a^* and b^* are colors. Then our method uses the a^*b^* plane of the CIE1976LAB color space. This color space can represent the color perception of a human to Euclidean distance, and we do not use the L^* factor to exclude the possible effect of illumination. In the first step, a simple clustering algorithm, such as the k-means algorithm, is used to obtain an over-segmentation of the image into N groups. Setting the nodes of the graph decides the average points of N groups. Then, we calculate the weight on each edge w_{uv} between all the nodes u and v.

$$w_{uv} = \exp\left(-\|I(u) - I(v)\|^2/\sigma_I^2\right) \times \begin{cases} \exp\left(-\|X(u) - X(v)\|^2\right)/\sigma_X^2), & \text{if } \|X(u) - X(v)\| < r \\ 0, & \text{otherwise} \end{cases} \quad (1)$$

where $I(u)$ and $I(v)$ are calculated from color values a^* and b^*. σ_I^2 is the variance of color distribution, and σ_X^2 is that of spatial distribution. Then, using edge weights w_{uv}, we calculate weight matrix W and diagonal matrix D[16].

Here we use a slight variation from a later paper by Fowlkes et al.[2]. In Eq. (2), $D^{-1/2}(D-W)D^{-1/2}$ is called the normalized Laplacian $\mathcal{L}$, and can be rewritten as follows:

$$\mathcal{L} = D^{-1/2}(D - W)D^{-1/2} = I - D^{-1/2}WD^{-1/2}. \quad (2)$$

By Eq. (2) is rewritten as

$$(D^{-1/2}WD^{-1/2})z = (1 - \lambda)z. \quad (3)$$

We can span a low dimensional space, of $E-1$ dimensions, with the eigenvectors from the $E+1$ least significant eigenvalues, where E is the partition number, and we ignore the least significant eigenvalue and the corresponding eigenvector. In the least significant space, all the input data have roughly same values due to the data normalization. We map the input data onto this low dimensional space,

$$y_{Eij} = z_{i+1,j}/\sqrt{D_{jj}}, \quad (i = 1, ..., E, j, ..., N,). \quad (4)$$

Finally, we can segment y_{Eij} into E clusters using the k-means method.

2.2 Color Restoration based on Spectral Information

The spectra obtained by a spectrometer depend on the illumination and object characteristics. Therefore, these spectra vary with a change in intensity and energy distribution of the light source, which are material characteristics. This

problem is called color constancy. Our method has a solution of color constancy by spectral information using a white reference[3]. This color, which is invariant to illumination, is applied to the color of the DSC image.

2.2.1 Illumination Color Change using Spectral Information

First, consider an opaque inhomogeneous dielectric object having diffuse reflection, and then the body reflection described by Shafer[15] as follows. Let $E(\vec{x},\lambda)$ be spectral power distribution of the incident light at the object surface at $\vec{x}$, and let $R(\vec{x},\lambda)$ be the spectral reflectance at the object surface at $\vec{x}$. The spectral sensitivity of the k-th sensor is given by $S_k(\lambda)$. Then, the sensor response of the k-th channel $I_k(\vec{x})$ is given by

$$I_k(\vec{x}) = G_B(\vec{x},\vec{n},\vec{s})\int_\lambda E(\vec{x},\lambda)R(\vec{x},\lambda)S_k(\lambda)\mathrm{d}\lambda, \tag{5}$$

where λ denotes the wavelength, $\vec{n}$ is the surface normal, and $\vec{s}$ is the direction of the illumination surface. The integral is taken from the visible spectrum (e.g., 380-780 nm). The geometric term G_B denotes the geometric dependency on the reflection.

Second, a white reference has the reflectance of a perfect diffuser. This reflects all wavelengths of the light source and does not absorb any of them. Hence, a white reference has spectral reflectance $R^w(\lambda) \cong 1$. Furthermore, we assume that the surface normal $\vec{n}$ is equal to lighting direction $\vec{s}$, then $G_B(\vec{x},\vec{n},\vec{s}) = 1$. The sensor response of the matte white reflectance allows us to rewrite Eq. (5) as

$$I_k^w(\vec{x}) = \int_\lambda E(\vec{x},\lambda)S_k(\lambda)\mathrm{d}\lambda. \tag{6}$$

In this way, the relative spectral power distribution of the white reference is measured.

Third, an object spectrum of an arbitrary sample is measured under the same illumination conditions. The k-th sensor response of a sample with respect to a white reference is given by

$$\frac{I_k(\vec{x})}{I_k^w(\vec{x})} = \frac{G_B(\vec{x},\vec{n},\vec{s})\int_\lambda E(\vec{x},\lambda)R(\vec{x},\lambda)S_k(\lambda)\mathrm{d}\lambda}{\int_\lambda E(\vec{x},\lambda)S_k(\lambda)\mathrm{d}\lambda}. \tag{7}$$

Through the use of the spectrometer, the filters $S_k(\lambda)$ are narrow-band filters. Let the filter $S_k(\lambda)$ be modeled as a unit impulse that is shifted over N wavelengths, the transmission at $\lambda_k = \delta$ and zero elsewhere. This allows us to rewrite Eq. (7) as

$$I_k(\vec{x})/I_k^w(\vec{x}) = (G_B(\vec{x},\vec{n},\vec{s})E(\vec{x},\lambda_k)R(\vec{x},\lambda_k))/E(\vec{x},\lambda_k) \tag{8}$$

obtaining

$$I_k(\vec{x})/I_k^w(\vec{x}) = G_B(\vec{x},\vec{n},\vec{s})R(\vec{x},\lambda_k). \tag{9}$$

Finally, the target color spectra $I_k'(\vec{x})$ are the product of Eq. (7) and the sensor response $I_k^{w'}(\vec{x})$ of the white reference under an arbitrary illumination. The equation is as follows:

$$I_k'(\vec{x}) = I_k(\vec{x})I_k^{w'}(\vec{x})/I_k^w(\vec{x}) = G_B(\vec{x},\vec{n},\vec{s})E'(\vec{x},\lambda_k)R(\vec{x},\lambda_k)S_k'(\lambda_k), \tag{10}$$

where $S_k'(\lambda_k)$ denotes the arbitrary spectral sensitivity of the k-th sensor. According to Eq. (7), the color itself depends on spectral reflectance whereas the brightness of the color depends on factor $G_B(\vec{x},\vec{n},\vec{s})$. However, since our method uses the brightness of the DSC image, then we assume that $G_B(\vec{x},\vec{n},\vec{s})$ corresponds to the brightness of the DSC image.

2.2.2 Combining Spectral Information and the DSC image

We calculate CIE tristimulus value CIEXYZ from sensor response $I_k'(\vec{x})$ in Eq. (10). Here, we measure the color in point of object surface by a spectrometer. Therefore, the color pixel $\vec{x}$ denotes color region $m = 1, 2, \cdots, N$, where N is the number of color regions. Also, the spectral sensitivity of the k-th sensor $S_k'(\lambda_k)$ is changed into CIE RGB color matching functions $\bar{x}(\lambda_k), \bar{y}(\lambda_k), and \bar{z}(\lambda_k)$. Using Eq. (10), this equation is as follows:

$$\begin{aligned}
X_{sp}(m) &= K\int_{\lambda_k} E'(m,\lambda_k)R(m,\lambda_k)\bar{x}(\lambda_k)\mathrm{d}\lambda_k,\\
Y_{sp}(m) &= K\int_{\lambda_k} E'(m,\lambda_k)R(m,\lambda_k)\bar{y}(\lambda_k)\mathrm{d}\lambda_k,\\
Z_{sp}(m) &= K\int_{\lambda_k} E'(m,\lambda_k)R(m,\lambda_k)\bar{z}(\lambda_k)\mathrm{d}\lambda_k,
\end{aligned} \tag{11}$$

$$K = 100/\int_{\lambda_k} E'(m,\lambda_k)\bar{y}(\lambda_k)\mathrm{d},\lambda_k \tag{12}$$

where K is a coefficient to normalize Y_{sp} to 100. Next, we calculate color differ-

Vol.2010-CVIM-172 No.37
2010/5/28

ences, $CIE\Delta E^*_{ab}$, from target color $X_{sp}(m), Y_{sp}(m), Z_{sp}(m)$ and the average of segmented image color $X_{img}(m), Y_{img}(m), Z_{img}(m)$. Using the method of subsection 2.2.3, we can find correspondences m of target colors and color segment images. In our method, the brightness of the target color coincides with the brightness of the segmented image. The equation is as follows:

$$X_{sp}(m) = X_{sp}(m)Y_{img}(m)/Y_{sp}(m), \quad Y_{sp}(m) = Y_{img}(m),$$
$$Z_{sp}(m) = Z_{sp}(m)Y_{img}(m)/Y_{sp}(m). \tag{13}$$

The transform vectors $X_t(m)$, $Y_t(m)$, and $Z_t(m)$ to apply the target color to the segmented image are given by

$$X_t(m) = X_{sp}(m)/X_{img}(m), \quad Y_t(m) = 1.0,$$
$$Z_t(m) = Z_{sp}(m)/Z_{img}(m). \tag{14}$$

Finally, the transform vectors $X_t(m)$, $Y_t(m)$, and $Z_t(m)$ are multiplied by all the pixels of the segmented image $X_{img}(\vec{x})$, $Y_{img}(\vec{x})$, and $Z_{img}(\vec{x})$.

$$X^{'}_{img}(m) = X_{img}(\vec{x})X_t(m), \quad Y^{'}_{img}(m) = Y_{img}(\vec{x}),$$
$$Z^{'}_{img}(m) = Z_{img}(\vec{x})Z_t(m). \tag{15}$$

When all the segmented images are synthesized, the result is transformed into RGB color.

2.2.3 Finding correspondence of the spectral information and segmented image

We need to find the correspondence between the spectral sensor response and segmented image so that their color difference is minimized. Therefore, we calculate the color difference, $CIE\Delta E^*_{ab}$, from the spectral sensor response and the average color of the segmented image. This is calculated from a^* and b^* color values in the CIELAB color space. The equation is as follows:

$$\Delta E^*_{ab} = \left[(a^*_{sp} - a^*_{img})^2 + (b^*_{sp} - b^*_{img})^2\right]^{1/2} \tag{16}$$

where a^*_{sp} and b^*_{sp} denote a^* and b^* values of the spectral response, a^*_{img} and b^*_{img} are a^* and b^* values of the average of the segmented image. Finding the smallest sets, we can find correspondences between spectral sensor responses and segmented images.

2.3 Experiments and Results

In this section, we describe two experiments we have conducted, accuracy color restoration of metamers, and application to digital archive contents. All experiments were performed using a DSC (Nikon D1-X), spectrometer (SpectraScan PR-650), and white reference (PhotoResearch SRS-3). Fig. 1 shows the equipment of our system. In these experiments, we used lights as follows: **D55** Light (day light 5500K :SERIC XC-100) and **A** light (tungsten light 2848K), **CW** (fluorescent lamp), **H** (2300K), **D50** in (day light 5000K: Sakata Inx Corporation SpectraLight III), real torch light, real sunset light, and incandescent light (5900K: PSR500WD). These illumination spectra are shown in Fig. 2.

Fig. 1 Equipment

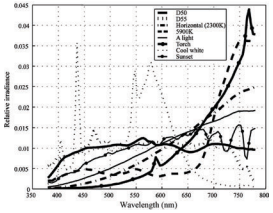

Fig. 2 Illumination spectra

2.3.1 Verification of Color Restoration Accuracy

In this experiment, we evaluated the color restoration accuracy of our method. We selected a target object that consists of five colors and has no specular reflection. First, we captured a target image under the D55 light. Simultaneously, we measured the spectral power distribution of colors of an object surface and a white reference using a spectrometer. We changed the color of the DSC image into the color under target illuminations by our method, where target illuminations were **A** light, **CW**, and **H**, described in the previous section.

Notice that the color of the output image Figs. 3. c at left is similar to that of ground truth Figs. 3. c at right. Table 1 shows the color differences, $\Delta E_{a^*b^*}$, between ground truths and restoration colors. Here, the ground truth of the target spectra is measured under several illuminations, and restoration colors are estimated values in the CIELAB color values. Notice that the average of the color differences, $\Delta E_{a^*b^*}$, between ground truths and restoration colors is less than 1.08 in the target object. Generally, in human vision, the color difference that enables us to discriminate between two colors is more than about 3.0.

2.3.2 Application to Digital Archive Contents

We made digital archive contents to evaluate the practicality of our method.

Fig. 3 Output image and ground truth. (a) Input image; (b) Segmentation result by NCuts method; (c)left column: simulated image under each light by our method; (c) right column: captured image under **A** light.

	Purple	Green	Skin	W and B	Average
A	0.282301	0.438471	0.968805	0.20786	0.474359
Cool White	0.788768	1.460883	1.895176	0.20272	1.086887
Horizontal	0.245402	0.284683	1.096399	0.33352	0.490001

Table 1 Color difference ($\Delta E_{a^*b^*}$) between restoration colors and ground truths

Benkei-ga-ana tumulus is an ancient tomb in Japan, made late in the 6th century. Several wall paintings resembling ships and horses were painted by ancient artists in this tumulus.

Notice that part of the red pigment can be extracted, as shown in Fig. 4. This object has an ambiguity of boundary caused by degradation of the wall painting. For this reason, we configured the parameter of NCuts to decrease the contribution of spatial distribution σ_X in Eq. (1) and increase the number of segments. The clear boundary of each segment cannot be observed, but we can extract relatively accurate pixels in the parts of the pigments in Fig. 4. b. Color transformation error could hardly be observed in Fig. 4. c and d.

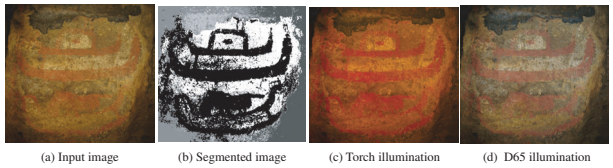

Fig. 4 Color restoration of a wall painting in the Benkei-ga-ana tumulus. (a) DSC captured image; (b)Segmented image (c) Simulated image under torch illumination; (d) Simulated image under D65 illumination

Archaeologically, we have a question as to how the artists painted the wall

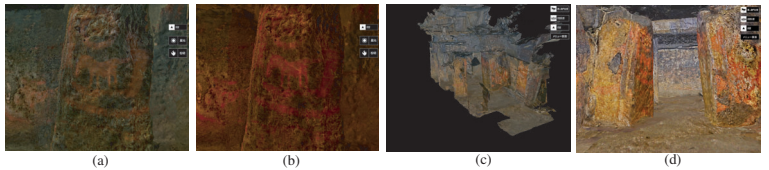

Fig. 5 Digital archive contents of Benkei-ga-ana tumulus (a) Simulation of color appearance under D65 light. (b) Simulation of color appearance under torch light. (c) Overview of Benkei-ga-ana tumulus. (d) Entrance of Benkei-ga-ana tumulus.

painting. We do not know whether they painted in daylight or using torch illumination. In Fig. 4, we are able to discriminate difference of colors under D65 (CIE daylight 6500K); however, under torch illumination, it is difficult for us to discriminate the color difference. Therefore, our assumption is that the artists made the wall paintings under D65 illumination. Fig. 5 shows the application of our method to digital archive contents. We restored more than 80 texture images in a content. Also, we found it possible to map the color restoration images onto 3D geometry by laser range sensor. This application behaves like virtual reality: we can interactively operate the viewpoint and change the illuminations.

3. Multispectral Imaging for Material Analysis in an Outdoor Environment

This section describes a new multispectral imaging system applicable to wide areas. Our design allows the system to have a wide field of view of high resolution with low noise and negligible distortion. We can apply this system to measuring the surface spectrum on an object surface in an outdoor environment. For determining the distribution of microorganisms, we developed a multispectral image segmentation method using the data obtained by our system. Finally, we applied our system and segmentation method to the data from the bas-relief of the Bayon Temple in the Angkor ruin, and we identified the classes and distribution areas of the microorganisms.

3.1 Acquisition of a Multispectral Image

We developed a novel multispectral imaging system that has a wide view angle, high image quality, and an accurate spectrum. The system can efficiently measure a target object in an outdoor environment.

3.1.1 Panoramic Multispectral Camera

Our multispectral imaging system has been designed to be a handy system with spectrum accuracy in each pixel with a wide view angle. The system consists of a small monochromatic CCD camera with a liquid crystal tunable filter (LCTF), shown in Fig. 6, mounted on an automatic pan/tilt platform (CLAUS Inc. Rodeon VR head). The LCTF (CRI Inc. Varispec) is an optical filter that allows the wavelength of the transmitted light to be electronically adjusted. The monochromatic CCD camera (Sony XCD-X710) with the LCTF mounted can obtain a series of two-dimensional spectral images by repeatedly changing the LCTF's transmittable wavelength with image acquisitions. The captured image has high image quality without distortion. The LCTF capturing system has a narrow field of view because the LCTF is mounted in front of the lens. We compensate for this problem by using an automatic panorama pan/tilt platform. The system captures a wide view multispectral image by synchronizing these three devices efficiently.

Fig. 6 Panoramic multispectral imaging system

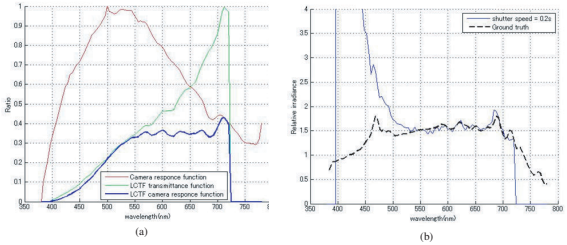

Fig. 7 (a) Spectral sensitivity function of monochromatic CCD camera and LCTF transmittance function (b) Illumination spectrum when the exposure time in all bands is fixed. (Black):obtained spectrum, (Blue):ground truth.

3.1.2 Estimation of Adaptive Exposure in an Outdoor Environment

The optimal exposure time is necessary to be determined in each wavelength due to the two reasons: uneven characteristics and varying illumination conditions. A multispectral imaging system using LCTF generally needs a fixed exposure time over the entire range of wavelengths for comparing pixel intensities over all wavelengths. However, the spectral sensitivity(blue line) given by the combination of LCTF and monochromatic camera is very low in short wavelengths (e.g., 400-500 nm), as shown in Fig. 7.(a), and relatively high in other wavelengths. If the pixel intensity at a certain wavelength would be smaller than the dark current noise, we would not be able obtain a meaningful measurement at that wavelength. For instance, Fig. 7.(b) shows a measured spectrum under dark illumination. Longer exposure time is necessary for spectral accuracy with wavelengths from 400 nm to 500 nm than for other wavelengths.

Varying illumination conditions occur in an outdoor environment, in which many cultural heritages are located. Our sensor samples spectral data by changing the LCTF's filtering characteristics and samples a series of images along the wavelengths. During this sampling period, it often occurs that the illumination condition varies due to the movement of clouds. If the intensity of illumination dramatically varies during measurement, it would induce saturation or underexposure at certain wavelengths. The dynamic determination of optimal exposure time at each wavelength is necessary for adjusting the effects of varying illumination conditions.

We attempt to estimate an optimal exposure time for each wavelength based on noise analysis[13]. The noise can be categorized into signal-dependent noise and signal-independent noise (SIN). In this system, we mainly consider the effect due to the signal-independent noise, since the signal-dependent noise is negligible compared with signal-independent noise. The signal-independent noise is composed of fixed pattern noise (FPN) and read-out noise, and photo response non-uniformity (PRNU). FPN is a dark current noise, a dynamic component. The read-out noise is composed of the reset noise, amplifier noise, and quantization noise. We focus on the FPN and the read-out noise, since PRNU is a static component easily calibrated in the initial stage.

The FPN depends on the temperature and the exposure time. Here, we assume that the sampling time is reasonably short, say 5 to 10 min, so that the temperature can be considered as constant. The FPN has a linear relation with the exposure time as shown in Fig. 8. The linear relation can be expressed as follows: $\epsilon_{DC} = at + b$, where t is an exposure time, a is the amount of the FPN increase depending on exposure times, and b is the amount of the FPN with zero

exposure time at that particular temperature. These values are measured at the site before sampling from a series of images with various exposure times while the lens is covered with a cup.

The read-out noise appears randomly at pixel positions at each image. We model the read-out noise as a Gaussian distribution at each pixel. In order to evaluate the parameters of the Gaussian distribution, we obtain a series of lens-covered images, and we calculate mean and standard deviation values. The mean value of images ϵ_{DC} are the FPN, and the standard deviation value of images ϵ_R are read-out noise. We use the upper bound of the SIN as $\epsilon_{DC} + \epsilon_R$.

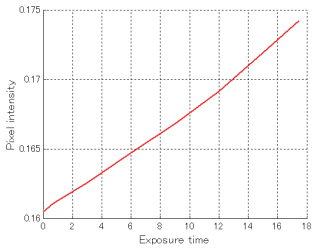

Fig. 8 The correlation between the FPN and exposure time.

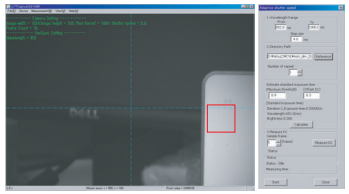

Fig. 9 GUI of panoramic multispectral imaging system.

Based on the discussion of the noise analysis, we design the procedure to determine the optimal exposure time at each wavelength. The procedure consists of two parts. The first part finds the exposure time that gives the brightest image of a white reference while avoiding saturation over all wavelengths. The second part determines any wavelength that gives lower value in the white reference than the SIN upper boundary, and, if this wavelength exists, it increases the exposure time while avoiding saturation.

The first part consists of:

Step 1. Select the brightest area ($m \times n$) on a white reference at each wavelength, λ, as shown in Fig. 9, and obtain the average brightness within the window, $L(\lambda)$. Repeat this step over all wavelengths

Step 2. Obtain the maximum value, L_{max}, among all the brightness values over all wavelengths.

Step 3. Determine the standard exposure time t_s as the longest exposure time when all the values in the brightest area found in Step 1 are not saturated. Namely, $L_{max} < 2^{16}$.

The second part rescues the particular wavelength image buried under the noise level. For this, we measure the FPN ϵ_{DC} and read-out noise ϵ_R by putting the cap in front of lens. Here, the average value is the FPN, and the standard deviation is considered as the boundary of the read-out noise.

In each wavelength, the optimal exposure time $t(\lambda)$ is adaptively estimated. The optimal exposure time $t(\lambda)$ can be represented as:

$$t(\lambda) = \begin{cases} t_s(\epsilon_{DC} + \epsilon_R + \mu)/L(\lambda) & (if\ L(\lambda) < \epsilon_{DC} + \epsilon_R + \mu) \\ t_s & (otherwise) \end{cases} \quad (17)$$

where μ is an off-set value to bring the adjustment to the safer side.

3.1.3 Multispectral Image Synthesis

After capturing images, we can synthesize the obtained images $L(i, j, \lambda)$ to the spectral power distribution image $L'(i, j, \lambda)$:

$$L'(i, j, \lambda) = t_s(L(i, j, \lambda) - \epsilon_{DC}(i, j, \lambda))/t(\lambda) \quad (18)$$

Here, the FPN image $\epsilon_{DC}(i, j, \lambda)$ in arbitrary exposure time can be estimated by using following equation, according to the linear correlation between the FPN and exposure time, as shown in Fig. 8:

$$\epsilon_{DC}(i, j, \lambda) = \alpha(\lambda)\epsilon^s_{DC}(i, j, \lambda), \quad (19)$$

where $\epsilon^s_{DC}(i, j, \lambda)$ is measured as the FPN image first. This can be obtained to calculate the mean image of captured images when light is intercepted from the camera. The linear correlation between the FPN and exposure time is as follows:

$$\alpha(\lambda) = (at(\lambda) + b)/(at_s(\lambda) + b), \quad (20)$$

where a and b are, respectively, slope and intercept.

We calculate a spectral power distribution image $L(i, j, \lambda)$, which is divided into the channel values $L'(i, j, \lambda)$ in each pixel i, j by camera sensitivity function $C(\lambda)$, and LCTF transmittance function $T(\lambda)$. Fig. 7 shows the actual sensitivity functions of each.

$$L(i, j, \lambda) = L'(i, j, \lambda)/(C(\lambda)T(\lambda)). \quad (21)$$

Next, we stitch the multispectral images of different view angles. Stitching usually extracts image features from a pair of images, establishes correspondences

among such extracted features, and calculates the translation and rotation parameters to superimpose overlapping areas for connecting these two images. Here, the features in multispectral images are different in each band image. To overcome this issue, we generate an intensity image using all the spectral images in each viewing direction. Second, we extract Scale-Invariant Feature Transform (SIFT) features (interest points)[10] from these initensity images and establish correspondences for obtaining the translation and rotation parameters. Finally, we stitch the spectral image of each view angle using these parameters. Fig. 10 shows a synthesized panoramic multispectral image.

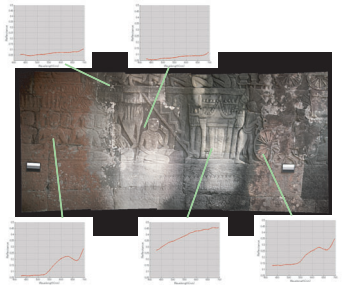

Fig. 10 Panoramic image made from multispectral images: this image has 81 dimensional spectrum in each pixel.

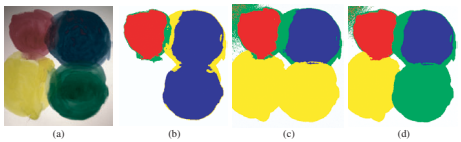

Fig. 11 Segmentation result of layered surfaces (a) Input image (b) Method 1: PCA + k-means (c) Method 2: KPCA + k-means (d) Method 3: Proposed NCuts on super-pixel method

3.2 Multispectral Image Segmentation

Segmentation of a multispectral image needs dimensional reduction. For dimensional reduction, linear and nonlinear reduction methods exist. Our prime objects, microorganisms on the bas-relief of the Bayon temple, have a nonlinear characteristic in spectral distributions due to the combination of top and bottom layers. Consequently, we need to employ the nonlinear demension reduction method. We develop a multispectral image segmentation method using NCuts.

3.2.1 Nonlinear Mixing and Layered surfaces

Some of the top layer's pixel spectra typically show mixed spectral characteristics between the top layers and bottom layer. These cause a so-called spectral mixing[5]. The spectral mixing can be categorized into two models: linear mixing and nonlinear mixing. The linear mixing occurs when one pixel consists of sub-parts from different materials; the different materials are distributed on the image plane. Generally, the linear mixing can be solved by reducing spectral dimension by using PCA, and clustering reduced data.

Our application, analysis of microorganisms, falls in the category of nonlinear mixing problem. This mixing occurs due to layer surfaces such as microorganisms and bottom rock surfaces. The different half-transparent materials are distributed along the line of sight. The PCA method cannot be applied to nonlinear mixing, but the nonlinear mixing problem can be solved either by employing the extending the kernel PCA (KPCA)[14] or the NCuts method.

3.2.2 Dimension Reduction of Normalized Cuts

The dimension reduction of NCuts is similar to it of KPCA. KPCA is a typical kernel method. KPCA projects high-dimensional space to lower-dimensional space, using eigenvalue decomposition based on the Gram matrix. NCuts method employs the Laplacian matrix, instead of the Gram matrix, for nonlinear mapping from input data and Gaussian Kernel, and then finds the optimal lower-dimensional space using eigenvalue decomposition.

We prefer the NCuts method over the KPCA because of computational cost. KPCA needs more dimensions for effectively representing data, because typically a cumulative curve is rather flat in KPCA; there is not much difference in the contribution between two adjacent eigenvalues. On the other hand, in the NCuts method, once we find the partition number, indicating how many regions exist in an image, we only need to pick up n eigenvectors in ascending order, where n is the partition number. In our application, it is relatively easy to set the partition number as a rough estimation of how many regions of microorganisms exist in the scene. For this reason, we prefer the NCuts method to KPCA for our nonlinear segmentation.

The NCuts method consists of nonlinear dimension reduction and clustering. Among various segmentation methods, the Ncut method has a unique feature of nonlinear dimensional reduction.

3.2.3 Applying NCuts to multispectral segmentation

Dimensionality is one of the issues in applying the NCuts method to the mul-

tispectral image segmentation method. The NCuts method requires making a weight matrix of a high-resolution image, of which the dimensions are $(N \times N)$, where N is the number of image pixels, typically more than 250,000. The NCut method handles this issue by effectively using the proximity threshold, ignoring remote nodes for calculation, and ending up solving a sparse matrix of a high-dimensional image.

We employ a two-step method to overcome this high-dimensional issue. In our microorganism analysis, we cannot apply the proximity threshold because two remotely located regions from the same kind of microorganism should be classified into the same class. We assume that a nonlinear manifold of high dimension has a linear sub-space in a low dimension. First, we over-segment the multispectral image using a standard PCA method and k-nearest neighbor method, and form super-pixels corresponding to each segment. Then, we apply the NCuts method to these super-pixels.

Our implementation is as follows: First, we compute M super-pixels by over-segmentation using PCA dimension reduction and k-nearest neighbor method. Second, we calculate M mean spectra for all M super-pixels. Let $I = \{I_1, I_2, I_3, ., I_i, .., I_M\}$, where I is spectrum data of m dimensional. Third, we compute the weight matrix W from $M\,(M < N)$ super-pixel values using the following equation:

$$W_{ij} = exp\left(-\|I(i) - I(j)\|^2/t^2\right) \tag{22}$$

In our experiment, we set t, a normalization factor, at 70% of the maximum distance in the weight graph. Finally, we can segment a multispectral image into material regions by using this weight matrix and NCuts.

3.3 Experimental Results

In this section, we describe two experiments. We conducted accuracy verification of our system, and applied our method to the analysis of cultural heritages.

3.3.1 Accuracy Verification of Multispectral Image

In this experiment, we captured multispectral images of a color chart (X-lite Color checker), under artificial sunlight (Seric XC-100), by using both fixed exposure and the proposed dynamic exposure methods, respectively. Then, we measured the spectrum of each patch using a spectrometer (PhotoResearch PR-655) as the ground truth. Next, we calculated the root mean square error (RMSE) between the obtained spectral data and the ground truth in each patch. Compared with the RMSE values by the fixed exposure method, the RMSE values by the proposed method are much lower. The mean value of RMSE in fixed exposure is 1.352. And the mean value of RMSE in the proposed dynamic exposure is 0.854. The result also showed that our system is effective for spectral analysis.

3.3.2 Comparison with Conventional Segmentation Method

In this subsection, we compared conventional segmentation methods and the proposed method. First, we calculated reflectance spectra from the input multispectral image by using our method. Second, we segmented the reflectance spectra image into different materials using these methods:

(1) Method 1: PCA and k-means clustering
(2) Method 2: KPCA and k-means clustering
(3) Method 3: Proposed NCuts on super-pixel method

Fig. 11 shows the segmentation result of layered surfaces for examining the effect on the nonlinear mixture. The input image is a watercolor pigment painted on a white paper. This image has complex color between the top layer and the bottom layer. Fig. 11. b, by Method 1, and c, by Method 2, include significant segmentation error.

3.3.3 Spectral Analysis for Bas-relief at the Inner Gallery of Bayon Temple

This subsection describes how we applied our proposed multispectral imaging system and segmentation method to analyze a cultural heritage. At the Bayon Temple in Cambodia, microorganisms are one cause of deterioration in the inner gallery. Fig. 12 shows the microscope images of microorganisms observed at each spot. Due to deterioration, the detailed bas-reliefs on the walls are losing their shapes. We examined the kind, distribution, and reproductive cycle of the microorganisms to find an effective method to remove them. We assumed that some of them could be discriminated by detecting the absorbance spectra of photosynthetic pigments in them, and we found we could calculate absorbance from reflectance.

Fig. 13. a shows the image of the scene we observed. Then, we found correspondences among multispectral images in different seasons to the same area through 3D data. The results in Fig. 13.b show the measured absorbance spec-

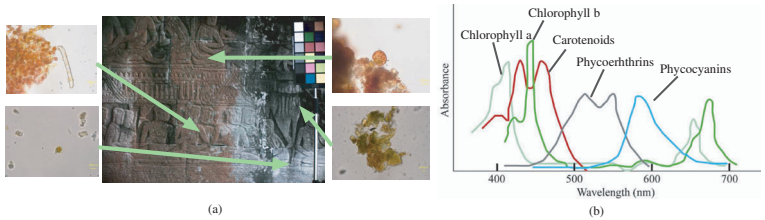

Fig. 12 (a) Microbial growth on the wall surface: microscope images of microorganisms observed at each spot.(b)Absorbance of photosynthesis pigments: green algae mainly has chlorophyll a and b. Cyanobacteria mainly has chlorophyll a and phycocyanins.

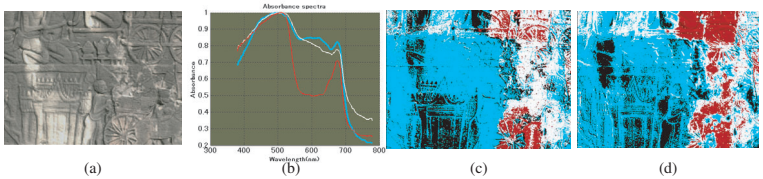

Fig. 13 (a) Observed scene image: this scene was made by mapping a multispectral image onto 3D data.(b)Absorbance spectrum in each class area.(c)Segmentation result of microorganisms in rainy season. (d)Segmentation result of microorganisms in dry season.

trum of each segmented area. The three areas, depicted using blue, white, and red colors in the figure, should be differentiated by the quantity of phycocyanin. This is because the areas' absorption has large differences at around 600 nm, which coincides with the phycocyanin's absorbance spectrum as shown in Fig. 12. As Fig. 13.c and d shows, white and blue areas decrease in a dry season compared to a rainy season, which implies that the quantity of phycocyanin has decreased in the dry season. The results indicate that the cyanobacteria, the main source of phycocyanin, increase in a rainy season and decrease in a dry season.

4. Decomposing Complex Reflection Components of a Layered Surface Using the Spider Model

In this section, we describe a novel physical model called the "Spider" model that can deal with color changes of layered surfaces and also decompose optical properties of each layers. The proposed model can represent the gradual color changes due to the change of optical properties of layered surfaces based on the Lambert-Beer (LB) based model. The proposed decomposition method cannot only segment the colors correctly even when they change gradually, but can also estimate the top layer's reflectance and optical properties, and the bottom layer's reflectance. Furthermore, there are no methods sharing our goals and techniques. We have developed methods for both an RGB image and a multispectral image.

4.1 Layered Surface Model

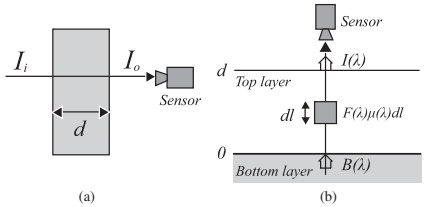

Fig. 14 (a) The optical model of the Lambert-beer model. (b) The optical model based on the Lambert-Beer model of layered surface objects

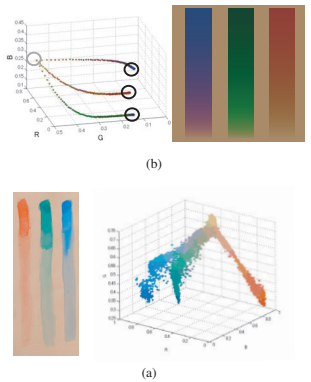

Fig. 15 Spider model:(a) (Left) Water color painting. (Right) The plot of left figure into the normalized color space. (b) Simulation of spider model: (Left) Simulated spider model. (Right) Simulated image.

The optical transmittance of light passing through a transparent object can be described by the Lambert-Beer Law[1]. It is the exponential function of the attenuation factor multiplied by the distance of the light traveling through the object, which is written as:

$$T(\lambda) = I_o(\lambda)/I_i(\lambda) = e^{-\mu(\lambda)d}, \tag{23}$$

where T is the optical transmittance, λ is the wavelength, I_o is the intensity of the outgoing light, I_i is the intensity of the incoming light, μ is the attenuation factor of the object, and d is the distance of the light traveling through the object

(the length of the light path). Assuming the light travels perpendicularly to the object surface, d can represent the optical thickness of the object. Fig. 14. a shows the pictorial description of the law.

The light reflected from layered surfaces can be modeled based on the Lambert-Beer law, which in this paper we call the Lambert-Beer based model, or LB-based model. First, let us consider the reflection from the bottom layer. The light reflected from the bottom layer is attenuated during the travel through the top layer; thus, the light received by the sensor becomes $B(\lambda)e^{-\mu(\lambda)d}$ from Eq. (23). B is the reflected light at the bottom layer, μ is the attenuation of the top layer, and d is the thickness, as illustrated in Fig. 14. b.

The light that is reflected by pigments of the top layer in the infinitesimal distance dl is $F(\lambda)\mu(\lambda)dl$, according to the definition of attenuation[12]. Here, we assume that pigments receive the same amount of light F in the top layer. The total amount of light reflected by the top layer is the sum of the light coming from each infinitesimal distance dl, which is the integration over the distance d: $\int_0^d F(\lambda)\mu(\lambda)e^{-\mu(\lambda)l}dl = F(\lambda)(1 - e^{-\mu(\lambda)d})$. Note that each light from dl is attenuated by the factor of $e^{-\mu l}$ by other pigments.

Thus, the total amount of light observed by the sensor becomes

$$I(\lambda) = B(\lambda)e^{-\mu(\lambda)d} + F(\lambda)\Big(1 - e^{-\mu(\lambda)d}\Big), \tag{24}$$

where I is the mixture intensity of the transmitted light from bottom and top layers. We call I a mixed layer. B and F can also be defined as the intensity of light coming from the surface when the thickness d is zero and infinitely large (∞), respectively. In this paper, we define opacity $\phi(\lambda) = 1 - e^{-\mu(\lambda)d}$. Hence, if we have two-layered surfaces, they are composed of the bottom layer $B(\lambda)$, the top layer $F(\lambda)$, and the opacity of the top layer $\phi(\lambda)$. This paper assumes that the opacity of the bottom layer is infinitely large throughout the image.

In more details, there are two types of bottom layers. The first is the bottom layer that is not covered by the top layer. This bottom layer receives light directly from the light source, which mathematically can be described as:

$$B'(\lambda) = L(\lambda)\rho(\lambda), \tag{25}$$

where B' is the reflection of the bottom layer when it is not covered by the top layer. L is the light intensity. ρ is the albedo of the bottom layer.

The second type is the bottom layer covered by the top layer, which we can formulate as:

$$B(\lambda) = L(\lambda)e^{-\mu(\lambda)d}\rho(\lambda), \tag{26}$$

and differs from Eq. (25) due to the change of the light impinging on its surface ($L(\lambda)e^{-\mu(\lambda)d}$). Note that in the last equation, we ignore the cumulative reflections reflected back and forth from the bottom layer to the top layer (the interface reflections), since we assume that the top layers are sufficiently thin.

4.2 Spider Model

Pixel values of a layered surface distribute as a curved line in the RGB space. They resembles the shape of a spider when multiple lines are observed. This section introduces the spider model and shows the derivation of it using the LB-based model (Eq. (24)).

Let us start with an example. Fig. 15. a shows the plot of water color painitng into the RGB space. The gray circle represents the bottom layer's reflection. Black circles represent the top layer's reflection with the largest opacity value. As one can observe, the three top layers roughly form three non-linear lines in the space. They stretch from the pixel values that represent the top layers with the largest opacity to the pixel values representing top layers with less and less opacity, and end up by intersecting at the bottom layer where the opacities of the three top layers equal zero. Fig. 15. b shows a synthetic image generated by the LB-based model (right), and its plot into the color space (left). We plotted three colors with various opacity values. The gray circle represents the bottom layer's reflection. Black circles represent the top layer's reflection when the opacity=1.

Mathematically, we derive the spider model as follows. First, instead of using spectral data, we use RGB color data taken from an ordinary digital camera for which the gamma correction is set to off. The LB-based model for the RGB data, then, can be expressed as:

$$I_c(x) = B_c(x)e^{-\mu_c(x)d(x)} + F_c(x)\Big(1 - e^{-\mu_c(x)d(x)}\Big), \tag{27}$$

where index c represents one of the three color channels {r,g,b} and x is the spatial image coordinate. B_c is the reflection by the bottom layer. F_c is the reflection of the top layer when the thickness is infinitely large (or sufficiently large so that the bottom layer does not affect the top layer's reflection). In the last equation, we assume that the camera's color sensitivities follow the Dirac

delta function. For the sake of simplicity, we will omit x throughout the paper; however, unless it is stated otherwise, the variables should be considered to be dependent on x.

Considering the intensities in the red and green color channels, from Eq. (27), we can write:

$$I_r = B_r e^{-\mu_r d} + F_r(1 - e^{-\mu_r d}) \tag{28}$$
$$I_g = B_g e^{-\mu_g d} + F_g(1 - e^{-\mu_g d}). \tag{29}$$

In the two equations, all variables are dependent on the color channels except for d. Thus, by letting $\alpha_c = e^{-\mu_c d}$:

$$\begin{aligned} &-d = \ln(\alpha_c)/\mu_c \\ &\ln(\alpha_r)/\mu_r = \ln(\alpha_g)/\mu_g \\ &\alpha_r = \alpha_g^{\mu_r/\mu_g}. \end{aligned} \tag{30}$$

From Eq. (29), we know that:

$$\alpha_g = (I_g - B_g)/(F_g - B_g). \tag{31}$$

Substituting the last equation into Eq. (30), we can obtain:

$$\alpha_r = ((I_g - B_g)/(F_g - B_g))^{\mu_r/\mu_g}. \tag{32}$$

Finally, by plugging the last equation into Eq. (28), we can express the intensity of the red color channel as:

$$I_r = B_r + \psi_r(I_g - B_g)^{\gamma_r}, \tag{33}$$

where $\gamma_r = \mu_r/\mu_g$, and $\psi_r = (F_r - B_r)/(F_g - B_g)^{\gamma_r}$. Accordingly, we can apply to the blue color channels, resulting in the following equation:

$$I_b = B_b + \psi_b(I_g - B_g)^{\gamma_b}, \tag{34}$$

where $\psi_b = (F_b - B_b)/(F_g - B_g)^{\gamma_b}$, and $\gamma_b = \mu_b/\mu_g$. Eqs. (33) and (34) imply that the correlations of the intensities in different color channels are not linear. Fig. 15. a shows the plot of the intensities, I_c, of layered surfaces in the RGB space, which form curved lines as predicted by Eqs. (33) and (34).

This spider model is the core of our method, since by obtaining it, we are able to know the optical parameters of the layered surface, which in turn enables us to classify the color of the top and bottom layers of a pixel. Furthermore, using their properties, we can analyze opacities of layers, and also simulate the color changing depending on the top layer's thickness as shown in Fig. 15.a.

4.3 Estimating Optical Properties of Layered Surfaces

Given a single input image containing the mixture of bottom and top layers, this section shows how to extract the optical properties of layered surfaces based on the spider model. This process is possible to be fully automatic, for example by tracing every line distribution in the color space, similar to[?)]. However, in this paper, to show the effectiveness of the spider model, we utilize simple user interactions to brush rough areas where the top layers and background layers are present. The brushing (or scribling) can be as simple as drawing a line, as shown in Fig. 16. b.

Overall, our proposed method consists of two processes: (1) Extracting the spider model (ψ_c, γ_c), (2) Determining the value of B_c, F_c and ϕ_c of each pixel in the input image by using a graphical model. This process is similar to the problem of labeling pixels by using multiple labels.

4.3.1 Estimating Spider Model

The aim of this section is to discuss how we can extract the spider model's parameters (ψ_c, γ_c). We consider two of cases: (1) an input image with a single bottom layer and several top layers, (2) an input image with several top layers and several bottom layers. Note that, these cases are just examples of conditions where our method can work.

Fig. 16. a shows an example of case 1. We assume that from the user's scribble we can have parts of regions where the top layers are present and parts of the bottom layer's region. To have the spider model's parameters of each region, we plot the pixels that correspond to the scribble on the top layer, producing three indepedent distributions in the RGB space as shown in Figs. 16. c - e. Fitting the spider model onto each of the distributions according to Eq. (33) and (34), will give us the values of $\{\psi_c, \gamma_c\}$ for red, green, and blue top layers. To help estimate $\{\psi_c, \gamma_c\}$, we use Levenberg-Marquardt method. The same process also works for an input image that has a single bottom and a single top layer. Note that B_c is known, since we can obtain it from the bottom region marked by a user.

Fig. 17. a shows an example of case 2, an input with several top layers and several bottom layers. For this case, not only can we estimate $\{\psi_c, \gamma_c\}$ for every top layer, but also estimate the values of F_c. Since according to the spider model,

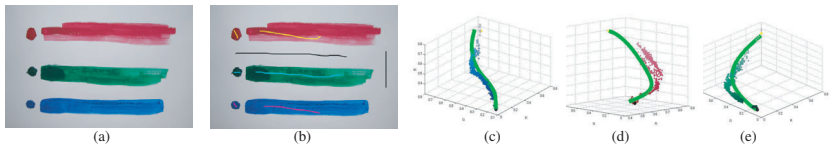

Fig. 16 Estimated spider model: (a) Input image. (b) Marked regions. (c) Estimated line of blue. (d) Estimated line of red. (e) Estimated line of green.

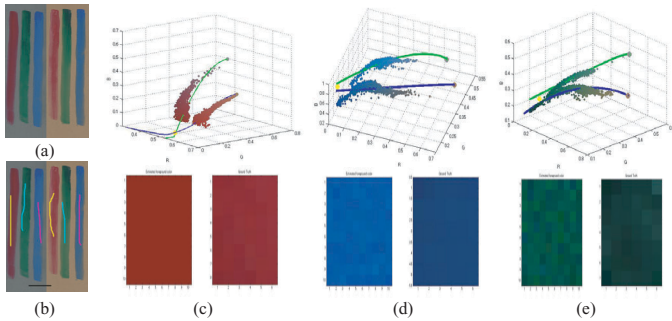

Fig. 17 Estimated spider model using the intersection of color lines. (a) Input image. (b) Marked regions (c) Red: (left) Estimated color lines, (right) Estimated color of the top layer and ground truth. (d) Blue: (left) Estimated color lines, (right) Estimated color of the top layer and ground truth. (e) Green: (left) Estimated color lines, (right) Estimated color of the top layer and ground truth.

if we have a top layer with two bottom layers, we will have two curve lines that intersect at a point representing opacity, $\phi_c = 1$. This phenomenon is shown in Fig.17. c until e. In the perspective of the spider model, the phenomenon also occur when we have two or more top layers and one bottom layer, where the intersection point indicates the reflection of the bottom layer B_c.

4.3.2 Layered Surface Decomposition

To decompose layered surfaces in an image is equivalent to estimating F_c, B_c, and ϕ_c for every pixel in the image. Therefore, given $\{I_x\}$, $\{B_c\}$, $\{w_l\}$, where index x represents an input-image pixel, I_x is the RGB values of pixel x, w_l is the curve line (or the spider's leg) generated by $\{\psi_c, \gamma_c\}$ of top layer l, we intend to estimate the label of x. In our case, the number of labels depends on the number of the top layers and the bottom layers, which is defined as $L = [1, \ldots, l, \ldots, N+1]$, where N is the number of the top layers, and $N+1$ is because we include the label of the bottom layer. For clarity, in this section we assume that we only use one bottom layer, although the method discussed below can also work for multiple bottom layers.

Solving this problem is also equivalent to computing the probability of the label of a pixel based on the distance between the pixel's RGB value and a leg of the spider model, where the leg represents the curve line that leads to the top layer. The closer the distance of a pixel to a leg, the higher the probability.

To correctly label the pixels, we should incorporate the case when a pixel is closed to the head of the spider model, meaning when a pixel is closed to a bottom layer. This can be solved by creating a data cost described as follows:

$$D(x = l|B_c, w_l, I_x) = \begin{cases} 0 & \text{if } d(I_x, B_c) < th \\ 1 - e^{-d(I_x, w_l)} & \text{otherwise} \end{cases} \quad (35)$$

where B_c is the RGB value of a bottom layer. w_l represents the curved line created by parameter $\{\psi_c^l, \gamma_c^l\}$. Function d represents the Euclidean distance in the RGB space. Threshold th is set depending on the noise level of the bottom layer and the camera, in our experiment we set the value between $10 \sim 20$ (within RGB standard values from 0 to 255). As the initial values, for all values of i and x, we set $D(x = l|B_c, w_l, I_x) = 1$.

Next, we also employ the smoothness constraint, and model the spatial correlations based on MRFs:

$$E\left(\{x\}, \{B_c\}, \{w_l\}, \{I_x\}\right) = \sum_p D(x = l|B_c, w_l, I_x) + \sum_{p,q} S(x_p, x_q)$$

where $S(x_p, x_q)$ will be zero if $x_p = x_q$, and one otherwise. To minimize the cost function, we use graphcuts for multiple labels[17].

Having labeled every pixel, we can now estimate the values of F_c, by analyzing the pixel distribution that are labeled to a top layer. F_c is the pixel that has the largest geodesic distance from B_c, since they are the edge points of the distribution. Finally, having estimated the values of F_c, we can straightforwardly compute the values of ϕ_c (the opacity) for every pixel. The Figs. 18 show decomposed images of Fig. 15.a.

Vol.2010-CVIM-172 No.37
2010/5/28

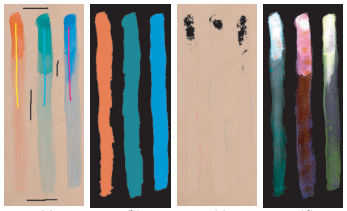

Fig. 18 The result of layered surface decompostion: (a) Input image with user specified top and bottom strokes. (b) Extracted top layer's image. (c) Extracted bottom layer's image. (d) Extracted opacity image $(1 - e^{-\mu d})$.

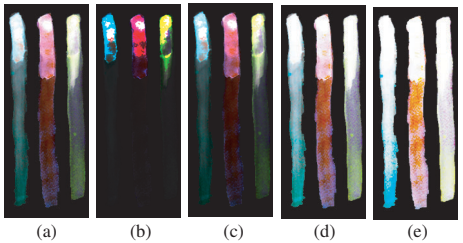

Fig. 19 (a) Estimated opacity image. (b) Reducing the opacity with n = 0.1. (c) Reducing the opacity with n = 0.5. (d) Increasing the opacity with n = 3. (e) Increasing the opacity with n = 9.

4.4 Simulation

Having decomposed the layers and extracted their optical properties, we are able to simulate the top layer's appearances with various degrees of opacity. If the estimated opacity image is represented as $\phi = 1 - e^{-\mu d}$, we can write: $e^{-\mu d} = 1 - \phi$. From section 4.1, we know that if we increase the opacity, optically it means we increase the optical thickness of the object. Thus, increasing the thickness n times implies $e^{-\mu n d} = (1 - \phi)^n$. Based on the last equation, we can simulate the opacity by using the following formula : $\phi' = 1 - (1 - \phi)^n$, where ϕ' is the simulated opacity, and n is a positive real number to change the thickness. We simulated the opacity of the water color painting in Fig. 15. a. Fig. 19. a shows the original estimated opacity, while Figs. 19. b-e show various simulated opacities. Note that the opacity is dependent on the wavelength, thus different color channels give different opacities, making the appearance of the opacity not white.

4.5 Experimental Results

4.5.0.1 Setup

In our experiment, we captured the images using NIKON D1X. The camera is radiometrically calibrated to obtain a linear correlation between the incoming light and the image intensities by setting the gamma correction off. We arranged the position of the light source distant from the objects, and we excluded the possibilities of shadows and interreflections. The regions of mixed layers and bottom layer in the captured image are roughly marked by user interaction. Then, optical properties of the layered surfaces are estimated.

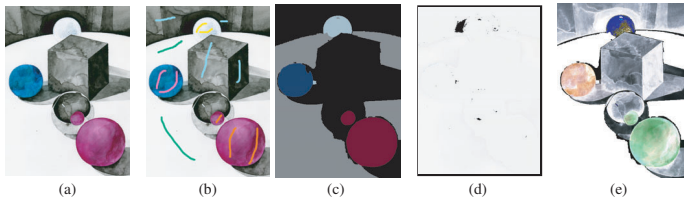

Fig. 20 (a) Input image: a water color painting painted by a professional artist. (b) Input image with user-specified top and bottom strokes. (c) Extracted top layers F_c. The region in gray is the pixels labeled as the bottom layer. Other colors represent the estimated top layer's color of each pixel. (d) Extracted bottom layer B_c. This is white since it represents the white canvas (e) Extracted opacity image ϕ.

4.5.0.2 Results

First, we demonstrate the application of layered surface decomposition to a water color painting in Figs. 20. Fig. 20. c represents the success of segmentation using a spider model. Next, as the results of being able to increase opacity synthetically, we can apply our method to increase the accuracy and robustness of color segmentation, particularly for objects with layered surfaces. Here, we will show the results of our segmentation based on our layered surface decomposition compared with the closed-form matting[8], an object segmentation method[9] and a k-means method. Fig. 21 shows the segmentation results of applying other methods to the images shown in Fig. 20. a and Fig. 22. a. Compared with our methods, these results are considerably less accurate and less robust. For these experiments, we used the Interactive Segmentation Tool-Box software (http://www.cs.cmu.edu/ mohitg/segmentation.htm) and matting software[8]. Finally, we conducted experiments simulating color change depending on various thicknesses of the top layer in Figs. 22.

In these results, we can simulate color change by various thicknesses of pigments. In Fig. 22. 2, we tried to recover some of the degraded parts of the wall painting. From the results, we could simulate color changes based on the various degrees of degradation.

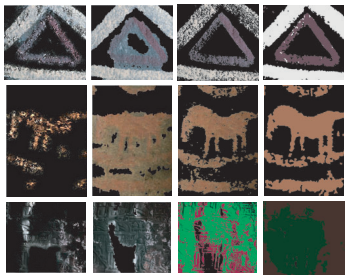

Fig. 21 Segmentation of layered surfaces: (a) Closed-form matting[8]. (b) Lazy Snapping[9]. (c) K-means. (d) Our method.

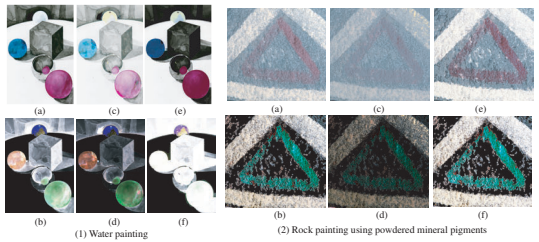

Fig. 22 Simulating color change of layered surfaces depending on various thicknesses of top Layers. (a) Input image. (b) Estimated opacity $1-e^{-\mu d}$ image. (c) Simulated image by reducing the opacity 10%. (d) Opacity image reduced 10%. (e) Simulated image increasing opacity 3 times. (f) Opacity image increased 3 times.

4.6 Extended method based on Spectral Information

So far, we described a proposed method based on RGB color. However, we can easily extend the method into a method based on spectral data. In this section, we describe in detail how to extend our method into a spectral-based method. Futhermore, we employ K/S values, which is the equation of the equation of Kubelka-Munk model[6]. We can estimate some wavelengths without scattering using the following equation:

$$K/S = (F(\lambda) - 1)^2/2F(\lambda), \tag{36}$$

where K is the absorption coefficient, and S is the scattering coefficient. When K/S is large, the scattering effect is small. In our experiment, the value of K/S is set at > 0.5. In this way, we can select optimal wavelengths without scattering. Let $I = I_1(\lambda), I_2(\lambda), \ldots I_i(\lambda), \ldots I_N(\lambda)$, where $I_i(\lambda)$ is an input spectrum of M dimension. $F_i(\lambda)$ is the reflectance spectrum of each top layer F_i. $B(\lambda)$ is the reflectance spectrum of a bottom layer. First, we can calculate the reflectance spectrum $B(\lambda)$ of the bottom layer and reflectance spectra of all top layers $F_i(\lambda)$ as well as we could using an RGB-based method. Second, we can estimate the M' optimal wavelengths by using K/S values. Furthermore, we select the wavelength m having most variance in their wavelengths. Then, we can select E dimensional wavelengths, which are consist of the m and arbitrary $E-1$ wavelengths. However, we do not need to estimate all forms of Eqs.37 for segmentation. We can select the number of wavelengths according to computational cost. Third, we estimate nonlinear lines having $E(E < M)$ dimension. It is necessary to use Eqs. (33), (34) for estimating nonlinear color lines. Then, we can rewritte Eqs. (33) and (34) as following the $E-1$ equations:

$$\begin{aligned} I(E) &= B(E) + \psi(E)(I(m) - B(m))^{\gamma(E)} \\ I(E-1) &= B(E-1) + \psi(E-1)(I(m) - B(m))^{\gamma(E-1)} \\ &\vdots \\ I(1) &= B(1) + \psi(1)(I(m) - B(m))^{\gamma(1)} \end{aligned} \tag{37}$$

Next, we segment spectra of each different layer. Finally, we can estimate $e^{-\mu(\lambda)d}$ in each pixel.

4.7 Experiment using Multispectral Image of Water Color Painting

In our experiment, we captured the multispectral image using the LCTF imaging system that is described in section 4.6. We also used artificial sunlight(Seric XC-100). Sample spectra were normalized by an illumination spectrum.

Figs. 23 show the RGB images of decomposed spectra and estimated spectra of each layer. The segmentation accuracy of these results compared favorably with the results of the RGB based-method. Fig. 23. e shows the comparison of between estimated spectra of top layers and ground truth, and also shows the K/S value of each pigment. Notice that blue and green results have sufficient accuracy, but the red result is less accurate. Fig. 23. b shows the K/S values of red pigment. Notice that K/S values are low in error wavelengths. This result implies that a scattering effect is affecting the wavelengths.

5. Conclusions

The ultimate purpose of this paper is the development of reflectance analysis methods using a multispectral image and yielding practical applications for modeling cultural heritages. Considering this purpose, the main contribution of this paper is to propose two multispectral imaging methods and two reflectance analysis methods. We apply these not only in theory but also in practice to show their viability. The contribution can be specifically summarized by the five following

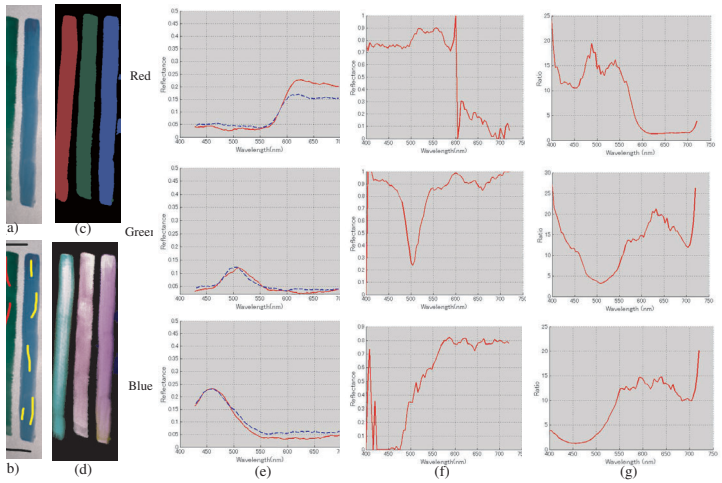

Fig. 23 Decomposed multispectral images. (a) Input image. (b) Scribbled image. (c) Estimated top layers image. For better visualization, we increased the brightness of the color. (d) Estimated $e^{-\mu(\lambda)d}$ image. (e) Estimated spectra of top layer. Red lines of (a), (b), and (c) are estimated spectra. Blue lines of (a), (b), and (c) are ground truth. (f) Estimated $e^{-\mu(\lambda)d}$ (g) K/S values in each spectrum.

points: First, we have developed a practical color restoration method based on spectral information for making VR contents, have actually produced VR contents by using restored images, and have also showed them in the Kyushu national museum. Second, we have developed a multispectral imaging system that can efficiently acquire spectra in a wide field. Third, we have proposed a multispectral image segmentation method based on statistical procedures. Fourth, we have proposed the Spider model as a physical model for layered surfaces, and have also proposed decomposing complex reflection components of a layered surface. Finally, we have applied our methods to both the reflectance analysis of tumuli and the spectral analysis of the bas-relief in the Inner Gallery of the Bayon Temple. These methods are specifically designed for modeling cultural heritages, but they can be used in other fields as well.

References

1) Beer, A.: Bestimmung der Absorption des rothen Lichts in farbigen flussigkeiten, *Ann. Phys. Chem*, Vol.86, No.2, pp.78–90 (1852).
2) Fowlkes, C., Chung, S. B.F. and Malik, J.: Spectral Grouping using the Nystrom Method, *IEEE Trans. on PAMI*, Vol.26, No.2 (2004).
3) Gevers, T., Stokman, H. M.G. and vande Weijer, J.: Color Constancy from Hyper-Spectral Data, *Proceedings of British Machine Vision Conference* (2000).
4) Ikari, A., Masuda, T., Mihashi, T., Matsudo, K., Kuchitsu, N. and Ikeuchi, K.: High quality color restoration using spectral power distribution for 3D textured model, *Proc 11th International conference on virtual system and multimedia* (2005).
5) Keshava, N. and F.Mustard, J.: Spectral Unmixing, *IEEE Signal processing magazine*, Vol.19, No.1, pp.44–57 (2002).
6) Kubelka, P. and Munk, F.: Ein Beitrag zur Optik der Farbanstriche, *Z. Tech. Phys*, Vol.12, pp.593–601 (1931).
7) lab, I.: Bayon Digital Archival Project.
8) Levin, A., Lischinski, D. and Weiss, Y.: A Closed form solution to natural image matting, *in proceedings of IEEE CVPR* (2006).
9) Li, Y., Sun, J., Tang, C. and Shum, H.: Lazy Snapping, *ACM Transactions on Graphics*, Vol.23, pp.303–308 (2004).
10) Lowe, D.G.: Distinctive image features from scale-invariant keypoints, *IJCV*, Vol. 60, No.2, pp.91–110 (2004).
11) Museum, T.N. and Toppan PrintingCo., L.: TNM and Toppan Museum Theater.
12) Nayar, S.K. and Narasimhan, S.G.: Vision in Bad Weather, *in proceedings of IEEE ICCV*, pp.820–827 (1999).
13) Reibel, Y., Jung, M., Bouhifd, M., Cunin, B. and Draman, C.: CCD or CMOS camera noise charactarisation, *The European Physical Journal Applied Physics*, Vol. 21, No.1, pp.75–80 (2003).
14) Schölkopf, B., Smola, A. and Müller, K.R.: Nonlinear component analysis as a kernel eigenvalue problem, *Neural Computation*, Vol.10, pp.1299–1319 (1998).
15) Shafer, S.: Using Color to Separate Reflection Components, *Color Research and Applications*, Vol.10, pp.210–218 (1985).
16) Shi, J. and Malik, J.: Normalized Cuts and Image Segmentation, *IEEE Trans. on PAMI*, Vol.22, No.8 (2000).
17) Szeliski, R., Zabih, R., Scharstein, D., Veksler, O., Kolmogorov, V., Agarwala, A., Tappen, M., and Rother, C.: A comparative study of energy minimization methods for Markov random fields, *in proceedings of ECCV* (2006).
18) Yamaguchi, M., Murakami, Y., Uchiyama, T., Ohsawa, K. and Ohyama, N.: Natural Vision: Visual Telecommunication based on Multispectral Technology, *Proc.IDW*, Vol.7, pp.1115–1118 (2000).